

ALIGN : Advanced Query Initialization with LiDAR-Image Guidance for Occlusion-Robust 3D Object Detection

Janghyun Baek¹, Mincheol Jang¹, Seokha Moon¹, Jinkyu Kim^{1*}, Seungjoon Lee²

¹Computer Science and Engineering, Korea University

²CTO Devision, LG Innotek

{2022020909, m1ncheoree, shmoon96, jinkyukim}@korea.ac.kr, lsj931228@lginnotek.com

Abstract

Recent query-based 3D object detection methods using camera and LiDAR inputs have shown strong performance, but existing query initialization strategies, including random and BEV heatmap-based sampling, still suffer from fundamental limitations. Random sampling uniformly distributes queries across the scene without object awareness, leading to inefficient focus and slow convergence. Heatmap-based sampling selects salient BEV regions but often overlooks occluded or small objects whose features are weak or invisible. To address this limitation, we propose **ALIGN** (Advanced query initialization with LiDAR and Image Guidance), a novel approach for occlusion-robust, object-aware query initialization. Our approach aligns 3D LiDAR geometry with 2D image semantics to estimate reliable object centers and adaptively place queries around them. In addition, it maintains a controlled budget of background queries to preserve global coverage, producing a tightly coupled routine that remains effective in both sparse and crowded scenes. Extensive experiments on the nuScenes benchmark show that ALIGN consistently improves performance across multiple state-of-the-art detectors, achieving gains of up to +0.9 mAP and +1.2 NDS, particularly under occlusion and dense traffic. Our code will be publicly available upon publication.

1 Introduction

Multi-sensor fusion based 3D object detection is a fundamental capability in autonomous driving and robotics, as it directly influences an agent's ability to perceive its environment, identify obstacles, and navigate safely in complex urban environments. Combining multiple sensor modalities, particularly LiDAR and cameras, has emerged as a preferred strategy to enhance detection robustness and accuracy [Liang *et al.*, 2018; Liu *et al.*, 2022b; Bai *et al.*, 2022; Huang *et al.*, 2024; Zhang *et al.*, 2024; Gong *et al.*, 2025]. While LiDAR provides accurate geometric, cameras offer rich semantic and texture cues, improving robustness under adverse lighting, heavy clutter, and occlusions.

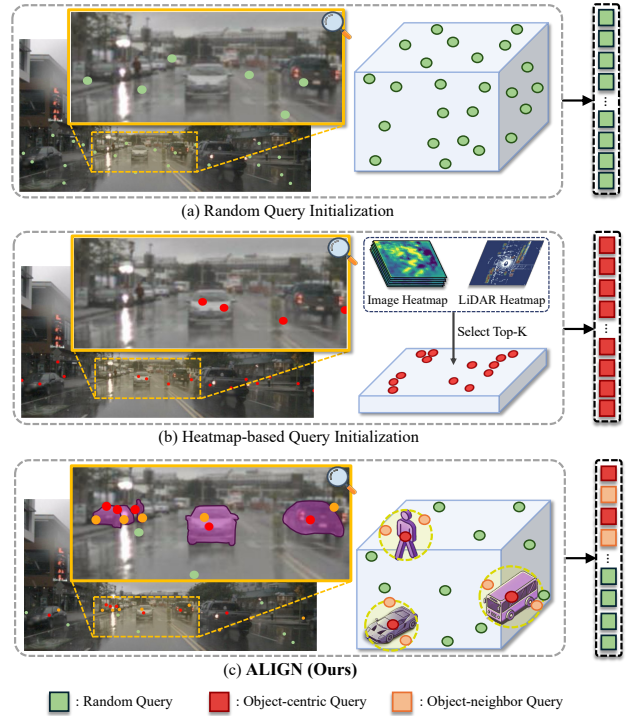


Figure 1: **Query Initialization Comparison.** Existing 3D object detectors typically adopt following query initialization schemes: (a) random initialization, where queries are sampled from uniformly distributed spatial regions, or (b) heatmap-based sampling from salient regions identified in BEV heatmaps. In contrast, (c) ALIGN accurately estimates object centers and samples queries in the vicinity of each center, while maintaining balanced background queries.

Recently, query-based methods [Gao *et al.*, 2022; Wang *et al.*, 2023; Zhao *et al.*, 2024] have shown strong performance by training each query to attend to potential objects in 3D space. However, their effectiveness largely depends on how queries are initialized. As shown in Fig. 1 (a) and (b), existing approaches mainly adopt two strategies: (1) Random sampling [He and Todorovic, 2022; Yan *et al.*, 2023b], which uniformly distributes queries without object awareness, leading to inefficient utilization, limited coverage, and slow convergence. (2) BEV heatmap-based sampling [Liu *et al.*, 2022b; Xie *et al.*, 2023], which allocates queries to top-K salient regions inferred from camera or LiDAR BEV heatmaps.

Since heatmaps primarily reflect strong visible responses, small or occluded objects often receive low confidence and are excluded. Consequently, both strategies struggle in complex urban scenes with large variation in scale and visibility.

To address these limitations, we introduce ALIGN, a novel object-aware query initialization strategy that aligns 2D image semantics with 3D LiDAR geometry to infer spatially and semantically consistent object centers (see Fig. 1(c)). Unlike BEV heatmap-based methods that infer query locations from coarse top-view confidence maps, ALIGN combines segmentation-guided projections with LiDAR-based clustering, enabling precise and robust query placement even for occluded, distant, or small objects.

ALIGN consists of three complementary modules for query initialization: (1) Occlusion-aware Center Estimation (OCE) estimates object centers by projecting LiDAR points onto image segmentation maps, combining geometric and semantic cues for localization under occlusion. (2) Adaptive Neighbor Sampling (ANS) enhances spatial coverage via LiDAR clustering and neighbor sampling within segmentation-consistent regions, enabling robust detection in crowded scenes. (3) Dynamic Query Balancing (DQB) preserves global coverage by retaining a limited number of background queries, preventing overfitting to dense object regions. These modules form a unified framework that improves localization accuracy and spatial coverage for more robust 3D object detection across diverse driving scenarios.

We evaluate our method on the widely used nuScenes benchmark [Caesar *et al.*, 2020], a large-scale autonomous driving dataset with multi-view cameras and LiDAR sensors. Since our approach integrates seamlessly into existing query-based detectors, we validate its generality across several state-of-the-art models, including CMT [Yan *et al.*, 2023b], TransFusion [Bai *et al.*, 2022], SparseFusion [Xie *et al.*, 2023], and FUTR3D [Chen *et al.*, 2022a]. Our model-agnostic design enables easy integration into a wide range of query-based detectors without modifying their core architectures. Extensive experiments show consistent improvements in both mAP and NDS, with particularly strong gains for occluded and small objects in crowded urban scenes.

Our main contributions are summarized as follows:

- We present ALIGN, a novel object-aware query initialization framework for multi-sensor 3D object detection that explicitly aligns 2D image semantics with 3D LiDAR geometry, enabling structured and object-centric query generation.
- We introduce three complementary modules (occlusion-aware center estimation, adaptive neighbor sampling, and dynamic query balancing) that collectively improve query localization, spatial coverage, and distribution balance across diverse driving scenarios.
- We demonstrate that ALIGN can be seamlessly integrated into various state-of-the-art query-based 3D object detectors, consistently yielding significant performance gains on the nuScenes benchmark, particularly under occlusion and crowding conditions.

2 Related Work

Recently, query-based 3D object detectors have shown strong performance using learnable queries that interact with multi-modal features. Their effectiveness mainly depends on how queries are initialized, which affects the model’s focus and convergence. Most approaches adopt one of two strategies: (i) random initialization and (ii) heatmap-based initialization.

2.1 Random Query Initialization

Most query-based 3D object detectors adopt random initialization following the DETR [Carion *et al.*, 2020] paradigm. DETR3D [Wang *et al.*, 2022] samples 3D reference points and aggregates image features via projection. PETR [Liu *et al.*, 2022a] introduces 3D position encoding into image features for implicit spatial grounding. FUTR3D [Chen *et al.*, 2023a] fuses image and LiDAR features at each query via a unified transformer without BEV or anchor priors. CMT [Yan *et al.*, 2023b] improves modality alignment via coordinate-aware position embeddings.

While simple and generalizable, random initialization leads to suboptimal query placement and slow convergence due to the lack of spatial and semantic priors. As a result, many queries fall into background regions, producing weak object cues and redundant attention. During early training, only a few queries receive positive supervision via Hungarian matching, while others remain unaligned or collapse onto the same salient regions. This inefficient allocation slows convergence and limits the discovery of small or occluded objects.

2.2 Heatmap-based Query Initialization.

To mitigate this issue, recent approaches adopt BEV heatmap-based initialization by sampling top- k salient regions. CenterFormer [Zhou *et al.*, 2022] selects object centers from BEV heatmaps and uses their voxel features as queries. TransFusion [Bai *et al.*, 2022] generates image-guided BEV heatmaps to initialize queries. SparseFusion [Xie *et al.*, 2023] samples queries from both image and LiDAR heatmaps, jointly guided by geometry and semantics. EfficientQ3M [Van Geerenstein *et al.*, 2024] combines BEV heatmaps with visual cues for query placement.

Although these methods improve query efficiency by focusing on likely object regions, they rely on strong visual or geometric responses in the BEV space. As a result, small or occluded objects with weak activations are often underrepresented, leading to missed detections in crowded scenes.

To address these limitations, we propose an object-aware and scene-adaptive query initialization strategy that leverages 3D LiDAR geometry and 2D image segmentation for robust 3D object detection. Our method estimates object centers via segmentation-guided projection and LiDAR clustering, and samples neighboring anchors within semantically consistent regions to capture local context. A fixed proportion of background anchors is retained to preserve global coverage and prevent overfitting to dense object areas. This design enables precise localization while maintaining scene coverage, improving detection of small and occluded objects.

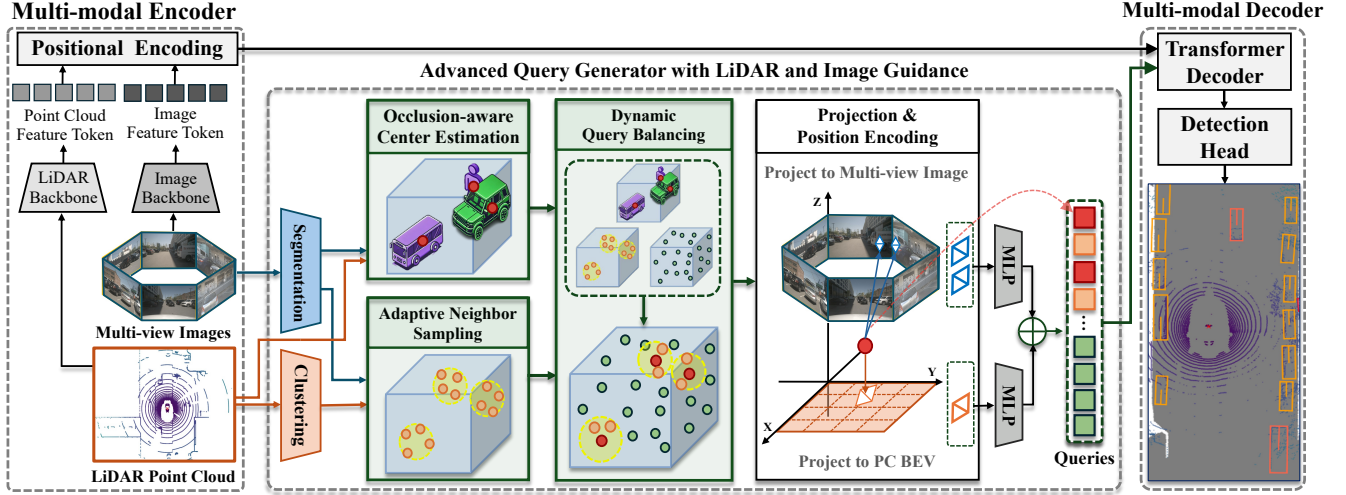


Figure 2: **An overview of ALIGN**, a novel query initialization strategy for query-based 3D object detection. Our framework consists of three components: (i) Occlusion-aware Center Estimation (OCE) for object center estimation from LiDAR point cloud and image segmentation, (ii) Adaptive Neighbor Sampling (ANS) for generating object candidates via LiDAR clustering and sampling object-aware queries, and (iii) Dynamic Query Balancing (DQB) for augmenting background queries to ensure a balanced foreground–background distribution.

3 Method

The overall framework of ALIGN is illustrated in Fig. 2. Given multi-view images and a LiDAR point cloud, ALIGN replaces heuristic query initialization with a structured generator that aligns geometric and semantic cues prior to transformer decoding. Specifically, ALIGN produces three types of query anchors: (1) Object-centric anchors from OCE, which estimate 3D centers by projecting segmentation-aligned LiDAR points with class-specific depth offsets. (2) Neighbor anchors from ANS, which sample semantically consistent points around clustered regions to recover occluded or truncated objects and (3) background anchors from DQB, which dynamically balance query allocation based on scene density. All anchors are encoded in image and BEV spaces and passed to the multi-modal transformer decoder, enabling improved spatial coverage and object localization.

3.1 Occlusion-Aware Center Estimation

To address the limitations of existing query initialization methods in localizing occluded, small, or sparsely sampled objects, we propose an Occlusion-Aware Center Estimation (OCE) module (Fig. 3(a)). OCE estimates 3D object centers by combining LiDAR geometry with image semantics at the point level. LiDAR points are projected onto image segmentation maps to associate each point with its visible instance, and the 2D–3D geometric relationship is used to estimate an approximate surface position. A class-specific depth offset is then applied to correct surface bias and obtain a more accurate 3D center, which serves as a stable, occlusion-aware anchor for query initialization. More implementation details and geometric interpretations of OCE are provided in the supplementary material.

3D LiDAR points (x, y, z) are projected onto the multi-view image planes, yielding image coordinates (u, v) via known calibration parameters. Let $\mathcal{M}_{i,j}$ denote the segmentation mask of the j -th object in the i -th view. We select only

the LiDAR points whose projections fall inside the segmentation mask $\mathcal{M}_{i,j}$ and define the set as $\mathbf{P}_{i,j}$:

$$\mathbf{P}_{i,j} = \{(u, v, x, y, z) \mid (u, v) \in \mathcal{M}_{i,j}\} \quad (1)$$

We select four LiDAR points closest to the center (u_c, v_c) of the 2D bounding box in image space to construct the set $\mathbf{S}_{i,j}$:

$$\mathbf{S}_{i,j} = \{\text{Top}_4(\mathbf{P}_{i,j}, \|(u, v) - (u_c, v_c)\|_2)\} \quad (2)$$

The bounding box center (u_c, v_c) is provided together with the segmentation mask $\mathcal{M}_{i,j}$ from the segmentation model. Using these, we estimate a local homography matrix $\mathbf{H}_{i,j}$ that maps image coordinates to LiDAR space:

$$[x, y, z]^\top = \mathbf{H}_{i,j}[u, v, 1]^\top. \quad (3)$$

Applying $\mathbf{H}_{i,j}$ to the 2D center (u_c, v_c) yields an approximate 3D points on the object surface, denoted as \mathbf{p}_{surf} :

$$\mathbf{p}_{\text{surf}} = \mathbf{H}_{i,j}[u_c, v_c, 1]^\top. \quad (4)$$

Although \mathbf{p}_{surf} corresponds to the visible surface, it does not coincide with the true geometric center due to its inherent surface bias. To compensate for this, we apply a class-specific *depth compensation offset* d , which approximates the displacement between the visible surface and the geometric center along the depth axis. This offset is applied along the LiDAR ray, yielding the final estimated center set:

$$\mathbf{P}_{\text{OCE}} = \left\{ \mathbf{p}_{\text{surf}} + d \cdot \frac{\mathbf{p}_{\text{surf}}}{\|\mathbf{p}_{\text{surf}}\|_2} \right\}. \quad (5)$$

3.2 Adaptive Neighbor Sampling

Although OCE reliably estimates object centers under occlusion, it depends on visibility and segmentation quality. When objects are heavily occluded or adjacent instances have unclear boundaries, segmentation masks may be missing or merged, leading to ambiguous localization. To address this, we introduce Adaptive Neighbor Sampling (ANS) (Fig. 3(b)),

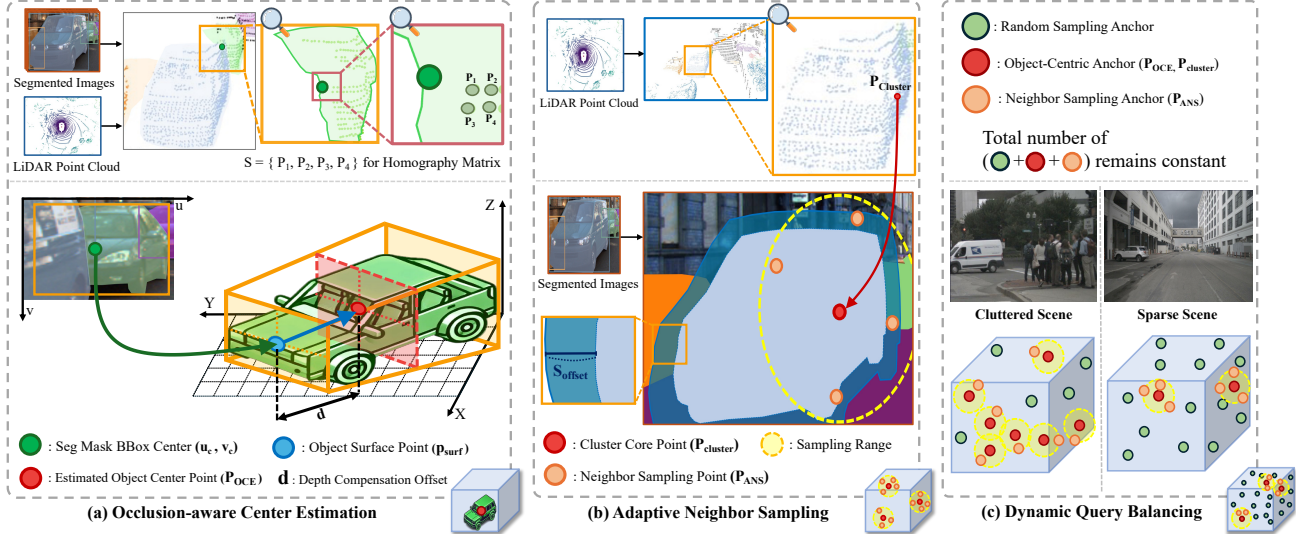


Figure 3: **Detailed illustration of each modules.** (a) OCE estimates object centers using LiDAR geometry and image semantics for robust localization under occlusion. (b) ANS samples segmentation-aligned neighbors around each LiDAR cluster core to expand anchor coverage. (c) DQB balances object-centric and background queries by scene complexity to preserve spatial coverage.

which leverages LiDAR clustering to identify object regions and samples neighboring points around each cluster core as query anchors. We apply DBSCAN [Schubert *et al.*, 2017] to cluster LiDAR points and use each cluster core $\mathbf{p}_{\text{cluster}}$ as an anchor. Following Deformable DETR [Zhu *et al.*, 2021], we randomly sample N neighbor points within a range r around each cluster core to capture object spatial extent.

$$\mathbf{P}_{\text{nbr}} = \left\{ \mathbf{p}_i \mid \text{dist}(\mathbf{p}_i, \mathbf{p}_{\text{cluster}}) < r, i = 1, \dots, N \right\}. \quad (6)$$

This naïve sampling include irrelevant regions such as walls or the ground. To mitigate this, we retain only points whose projections fall within a offset $\mathbf{S}_{\text{offset}}$ of the segmentation mask \mathcal{M}_i , forming the refined sampling set \mathbf{P}_{ANS} :

$$\mathbf{P}_{\text{ANS}} = \left\{ \mathbf{p}_i \in \mathbf{P}_{\text{nbr}} \mid \text{dist}(\Pi(\mathbf{p}_i), \mathcal{M}_i) < S_{\text{offset}} \right\}. \quad (7)$$

If the number of retained points in \mathbf{P}_{ANS} is insufficient, the sampling steps are repeated up to three times to ensure sufficient coverage. ANS complements OCE through geometry-based clustering and semantic filtering, ensuring reliable query initialization even when segmentation is incomplete or ambiguous, and producing the core anchor set $\mathbf{p}_{\text{cluster}}$ and the refined neighbor set \mathbf{P}_{ANS} . Detailed implementation of the DBSCAN-based LiDAR clustering and parameter settings used in ANS is provided in the supplementary material.

3.3 Dynamic Query Balancing

While OCE and ANS effectively generate object-centric anchors, assigning all queries to these regions may cause overfitting and limit generalization when some objects are missed. On the other hand, excessive background queries lead to redundant sampling in sparse areas with limited supervision. To resolve this trade-off, we introduce Dynamic Query Balancing (DQB) (Fig. 3(c)), which adaptively allocates remaining queries between object-centric and background anchors

based on scene complexity. After assigning object-centric anchors, the remaining queries are computed as :

$$N_{\text{ANS}} = \nabla_{\text{bal}} (N_{\text{total}} - N_{\text{OCE}} - N_{\text{cluster}}), \quad (8)$$

$$N_{\text{rand}} = (1 - \nabla_{\text{bal}}) (N_{\text{total}} - N_{\text{OCE}} - N_{\text{cluster}}), \quad (9)$$

where N_{total} denotes the total query budget, N_{OCE} and N_{cluster} denote the numbers of anchors from OCE and ANS cluster cores. $\nabla_{\text{bal}} \in [0, 1]$ is a fixed hyperparameter balancing object-centric refinement and background exploration. The remaining queries are divided into neighbor queries N_{ANS} and background queries N_{rand} . Neighbor queries are evenly allocated across object candidates, yielding fewer samples per object in crowded scenes to preserve background coverage and denser sampling in sparse scenes to improve localization.

3.4 Loss Functions.

We employ a simple loss composed of classification and 3D bounding box regression. Set prediction is optimized via Hungarian matching [Kuhn, 1955], with Focal loss [Lin *et al.*, 2017] L_{cls} for classification and L1 loss L_{reg} for box regression. The final loss is the weighted sum, as shown in Eq. 10. In all experiments, we set $\lambda_1 = 2.0$ and $\lambda_2 = 0.25$.

$$L_{\text{total}} = \lambda_1 L_{\text{cls}}(\mathbf{c}, \hat{\mathbf{c}}) + \lambda_2 L_{\text{reg}}(\mathbf{b}, \hat{\mathbf{b}}), \quad (10)$$

4 Experiments

4.1 Implementation and Evaluation Details.

Dataset and Metrics. We use nuScenes dataset [Caesar *et al.*, 2020] to evaluate our method’s effectiveness. The nuScenes dataset includes six cameras, five radars, and one LiDAR, offering a 360-degree field of view. The dataset contains 1,000 scenes split into 700/150/150 for training/validation/test and includes $\sim 1.4\text{M}$ annotated 3D bounding boxes covering 10 common object classes found in driving environments. We report mean Average Precision (mAP) and nuScenes Detection Score (NDS) as the main metrics.

Method	Query Init.			Validation		Test	
	Random	Heatmap	ALIGN	mAP↑	NDS↑	mAP↑	NDS↑
UVTR [Li <i>et al.</i> , 2022]	✓			63.9	69.7	65.4	70.4
Transfusion [Bai <i>et al.</i> , 2022]		✓		67.3	70.9	68.9	71.6
CMT-small [Yan <i>et al.</i> , 2023a]	✓			67.4	70.2	68.8	71.6
FUTR3D [Chen <i>et al.</i> , 2023a]	✓			67.4	70.9	69.4	72.1
EfficientQ3M [Van Geerenstein <i>et al.</i> , 2024]		✓		70.5	72.6	71.2	73.5
SparseFusion [Xie <i>et al.</i> , 2023]		✓		70.5	72.8	72.0	73.8
FocalFormer3D [Chen <i>et al.</i> , 2023b]		✓		70.5	73.1	71.6	73.9
CMT-Large [Yan <i>et al.</i> , 2023a]	✓			70.3	72.9	72.0	74.1
Transfusion + ALIGN			✓	67.7 (+0.4)	71.3 (+0.4)	—	—
CMT-small + ALIGN			✓	68.3 (+0.9)	71.4 (+1.2)	69.3 (+0.5)	72.2 (+0.6)
FUTR3D + ALIGN			✓	68.2 (+0.8)	71.8 (+0.9)	69.9 (+0.5)	72.6 (+0.5)
SparseFusion + ALIGN			✓	70.9 (+0.4)	73.1 (+0.3)	—	—
CMT-Large + ALIGN			✓	71.1 (+0.8)	73.3 (+0.4)	72.4 (+0.4)	74.5 (+0.4)

Table 1: Performance comparison on the nuScenes dataset. Replacing the original initialization with ALIGN consistently improves mAP and NDS across all baselines. The best results are highlighted in **bold**. All results are reported without test-time augmentation.

Method	Visibility		mAP (%)↑									Overall	
	Level	Num Obj.	Car	Truck	Bus	Tra.	Const.	Ped.	Moto.	Bike	Cone	Bar.	
CMT	1	23,437	49.7	8.40	15.5	17.6	4.30	56.8	41.7	19.0	20.5	25.6	25.9
CMT + ALIGN	(0–40%)	(19.2%)	51.1	9.97	18.3	17.8	4.75	57.6	44.1	21.3	22.4	25.8	27.3 (+1.4)
CMT	2	12,779	64.8	15.8	43.3	17.6	12.3	64.0	48.1	29.4	15.7	19.6	33.1
CMT + ALIGN	(40–60%)	(10.5%)	66.0	16.9	45.7	17.9	12.5	64.9	50.1	30.2	16.0	21.0	34.1 (+1.0)
CMT	3	17,815	79.3	40.4	65.5	31.2	25.2	71.0	73.5	48.5	29.2	44.2	50.8
CMT + ALIGN	(60–80%)	(14.6%)	79.9	40.9	66.3	32.0	25.3	71.7	74.7	50.1	30.3	45.5	51.8 (+1.0)
CMT	4	67,830	93.5	67.1	81.4	51.4	41.4	92.7	87.5	83.6	82.8	74.9	75.6
CMT + ALIGN	(80–100%)	(55.7%)	93.8	67.2	81.6	52.9	42.5	93.1	88.0	84.9	83.7	75.5	76.3 (+0.7)
CMT	Total	121,861	88.7	65.4	78.3	46.6	33.9	87.7	79.7	70.1	79.5	72.9	70.3
CMT + ALIGN	(0–100%)	(100%)	89.2	65.8	79.0	47.0	34.8	88.2	80.9	71.7	81.0	73.5	71.1 (+0.8)

Table 2: Detection performance across visibility levels on the nuScenes validation set using CMT-Large.

Implementation Details. We implement ALIGN on five query-based LiDAR-camera detectors and retain each baseline’s original backbone and training settings for fair comparison. Segmentation masks are generated by Mask R-CNN pretrained on nuImages, sharing the image backbone and performing FP16 inference at 800×320 resolution. The region of interest is set to $[-54, 54]$ m in X/Y and $[-5, 3]$ m in Z , and all feature and query embeddings use dimension $D = 256$. All models are trained for 20 epochs on $4 \times$ A6000 Ada GPUs using AdamW [Loshchilov and Hutter, 2019] with a cyclic learning rate policy [Smith, 2017] and weight decay of 1×10^{-2} . We employ CBGS [Zhu *et al.*, 2019] and AutoAlign [Chen *et al.*, 2022b] to address class imbalance.

4.2 Experimental Results

Quantitative Results. Table 1 reports the performance of five query-based LiDAR-camera detectors on the nuScenes validation and test sets before and after applying ALIGN. Across all baselines, ALIGN consistently improves both mAP and NDS, demonstrating its general applicability. The largest gains are observed when ALIGN replaces random initialization, which lacks spatial priors, with semantically grounded and geometry-aware object anchors. For example, CMT-small improves from 67.4 to 68.3 mAP (+0.9) and from 70.2 to 71.4 NDS (+1.2), while FUTR3D achieves +0.8 mAP and +0.9 NDS. In contrast, heatmap-guided methods such as TransFusion and SparseFusion show smaller yet con-

sistent gains (+0.4 mAP / +0.4 NDS), as they already leverage BEV-based spatial cues during initialization. The best-performing model, CMT-Large, reaches 71.1 mAP and 73.3 NDS, confirming that ALIGN scales effectively to larger architectures. Overall, replacing heuristic or random initialization with structured, semantically grounded anchors leads to more reliable query allocation and consistent performance gains. Additional segmentation robustness analysis is provided in the supplementary material.

Performance across Visibility Levels. The nuScenes benchmark categorizes objects into four visibility levels, from Level 1 (0–40%, heavily occluded) to Level 4 (80–100%, fully visible), based on 2D bounding box visibility. In the validation set, 19.2% of all instances fall into Level 1, indicating that heavily occluded objects are common in urban scenes. Table 2 reports class-wise mAP across visibility levels using CMT-Large as the baseline to analyze the impact of ALIGN under varying visibility conditions. As expected, baseline performance degrades as visibility decreases (Level 4 \rightarrow Level 1), while replacing the original query initialization with ALIGN consistently improves mAP at all levels, with larger gains under heavier occlusion (e.g., +1.4 at Level 1 vs. +0.7 at Level 4). Notably, significant improvements are observed for small and thin categories such as *Bicycle* (+1.6) and *Traffic Cone* (+2.2) at low visibility, highlighting the practical benefit of ALIGN in urban scenes.

	OCE	ANS	DQB	mAP↑	NDS↑	Lat.(ms)	Mem.(MB)
(a)				67.4	70.2	163	2812
(b)	✓			68.0	70.8	190	4066
(c)		✓		67.6	70.5	187	3084
(d)	✓	✓		68.2	71.2	215	4360
(e)	✓	✓	✓	68.3	71.4	215	4360

Table 3: Ablation of ALIGN modules on CMT-small

Depth Compensation Offset d	mAP↑	NDS↑
—	67.4	70.2
[0,0,0,0,0,0,0,0,0]	67.9	70.5
[1,2,2,2,2,0,0,0,0]	67.9	70.6
[1.5,3,3,3,3,0,0,0,0]	68.0	70.8

Table 4: Ablation of depth offsets in OCE.

Ablation of ALIGN Modules. Table 3 presents the ablation study on CMT-small using the nuScenes validation set. Adding OCE improves performance to 68.0/70.8 (mAP/NDS) by providing more reliable, segmentation-guided center localization. Using ANS alone reaches 67.6/70.5, indicating that adaptive sampling around LiDAR clusters partially compensates for missing center priors, though the fixed neighbor budget limits its effect. Combining OCE and ANS further improves performance to 68.2/71.2, showing their complementary roles in precise localization and adaptive spatial coverage. Finally, introducing DQB achieves the highest result (68.3/71.4), yielding total gains of +0.9/+1.2 over the baseline by balancing object-centric and background queries and preventing dominance by overrepresented regions. Overall, each module contributes complementary benefits, forming a unified framework that progressively improves detection performance.

Depth Compensation Offset in OCE. In OCE, LiDAR-based center estimation relies on visible surfaces from image-guided segmentation. Since LiDAR observes only object surfaces, the estimated centers may deviate from the true geometric centers, especially for large or elongated objects such as trucks and construction vehicles.

To mitigate this issue, we introduce a class-specific depth compensation offset d along the LiDAR ray toward the object interior. Following QAF2D [Ji *et al.*, 2024], the offset is derived from dataset-level 3D box size statistics of each class, providing a data-driven correction rather than heuristic tuning. Detailed derivation and class-wise offset ranges are provided in the supplementary material.

Table 4 reports ablation results for different offset settings. Compared to the baseline without OCE and the zero-offset variant, applying non-zero offsets consistently improves both mAP and NDS. Among the evaluated configurations, the dataset-informed offset [1.5, 3, 3, 3, 3, 0, 0, 0, 0, 0] achieves the best performance (68.0 / 70.8 mAP / NDS) and is adopted in our model.

Sampling Range and Offset in ANS. Table 5 reports the ablation results of the sampling range and offset in the ANS module. The sampling range is defined as a ratio of the Region of Interest (ROI) within $[-54, 54]$ m, where 0.030 corresponds to approximately 3.24 m and determines the spa-

Sampling Range	Sample Offset	mAP↑	NDS↑
—	—	67.4	70.2
0.015	15	67.5	70.3
0.015	30	67.6	70.5
0.030	15	67.5	70.4
0.030	30	67.6	70.5

Table 5: Effect of sampling range and offset in ANS.

∇_{balance}	N_{ANS}^{\max}	N_{rand}^{\max}	mAP↑	NDS↑
0.32	288	612	65.1	69.3
0.16	144	756	68.1	71.2
0.08	72	828	68.3	71.4
0.04	54	846	68.2	71.2

Table 6: Effect of balancing parameter in DQB.

tial extent for neighbor selection around each LiDAR cluster. A range of 0.015 already provides sufficient local coverage, and increasing it to 0.030 yields only marginal improvement, indicating that most relevant geometry is captured within a compact neighborhood. The offset controls how many pixels beyond the segmentation mask are included during neighbor aggregation. Larger offsets consistently improve mAP and NDS by slightly expanding the sampling boundary, allowing valid points near object boundaries to be included and leading to more reliable query initialization for partially occluded or irregularly shaped objects.

Balancing Parameter in DQB. Table 6 analyzes the effect of the balancing coefficient ∇_{balance} in the DQB module, where a total of 900 queries is used. After assigning OCE-estimated centers and ANS cluster cores as query anchors, DQB allocates the remaining queries between object-centric and background regions. The coefficient ∇_{balance} controls the maximum ratio of object-centric queries by defining upper bounds N_{ANS}^{\max} and N_{rand}^{\max} , while the actual numbers adapt dynamically to scene density. Performance peaks at $\nabla_{\text{balance}} = 0.08$ ($N_{\text{ANS}}^{\max} = 72$), achieving 68.3 mAP / 71.4 NDS. Larger ratios (e.g., 0.16 or 0.32) allocate excessive object-centric queries, leading to redundant representations and reduced background coverage, while smaller ratios (e.g., 0.04) limit the model’s ability to represent object regions effectively. These results indicate that $\nabla_{\text{balance}} = 0.08$ provides the best trade-off, maintaining balanced query allocation across varying scene complexities and stabilizing detection performance.

Analysis of Computational Overhead. We evaluate the computational overhead of ALIGN on the nuScenes validation set with CMT-small as the base detector, using a single NVIDIA A6000 Ada GPU. Table 3 summarizes the average inference latency per sample and GPU memory consumption. OCE introduces moderate overhead (+27 ms, +1254 MB) thanks to segmentation-guided center estimation using shared image backbone features. ANS adds minor overhead (+24 ms, +272 MB), as clustering and neighbor sampling operate on a sparse set of LiDAR points and are executed on the GPU. DQB incurs negligible overhead, as it only redistributes foreground and background queries without additional feature extraction. Overall, ALIGN achieves consis-

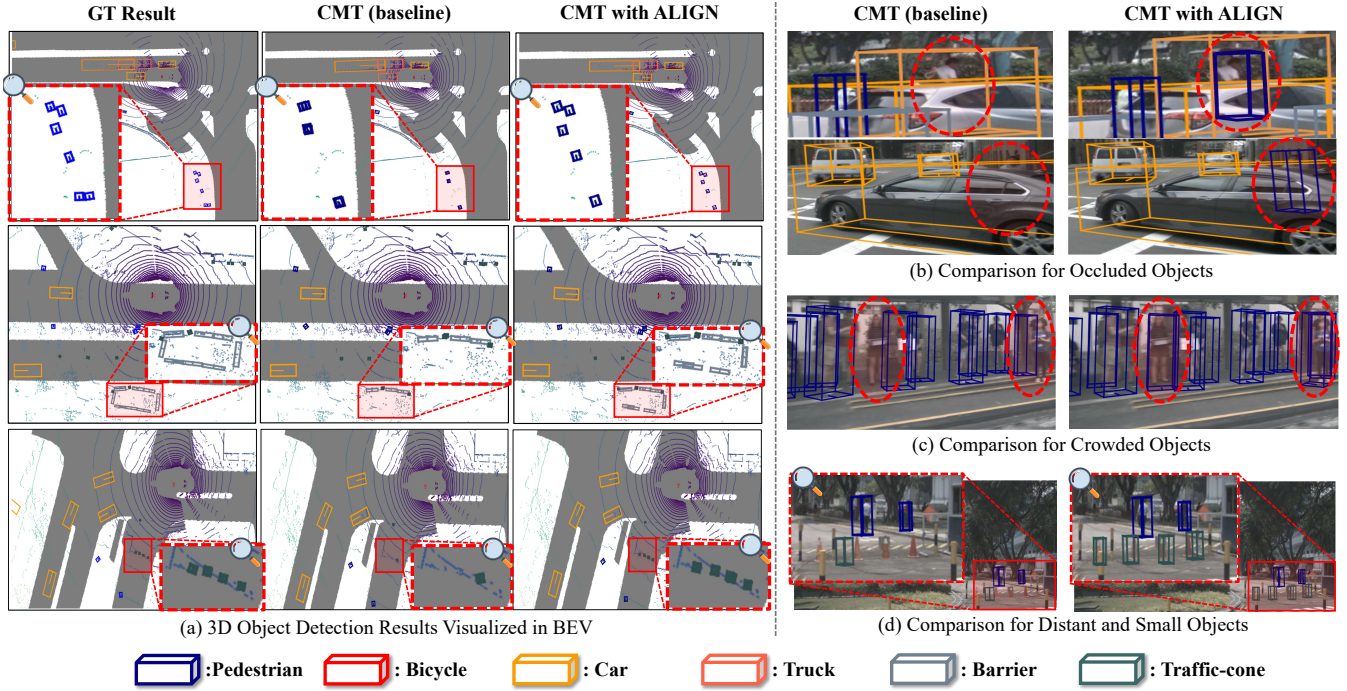


Figure 4: **Qualitative Comparison with and without ALIGN.** (a) BEV visualizations show that ALIGN improves localization of small and occluded objects, reducing missed detections and refining box placement. (b) Our method detects heavily occluded pedestrians missed by the baseline. (c) In crowded scenes, ALIGN better resolves overlaps, improving object separation and robustness. (d) Detection is more accurate for distant and small objects. Red dotted regions highlight areas where ALIGN outperforms the baseline.

tent accuracy improvements with modest computational overhead, making it suitable for practical deployment.

Qualitative Results. Figure 4 presents qualitative comparisons on the nuScenes validation set, illustrating how ALIGN improves detection robustness under diverse and challenging scenarios. As shown in Fig. 4(a), BEV visualizations reveal higher localization accuracy and recall, particularly for small or partially visible objects. This improvement is attributed to ALIGN’s structured query initialization, which integrates geometric priors, adaptive spatial sampling, and balanced query allocation, leading to more accurate and spatially consistent query placement across the scene. Figure 4(b) shows that ALIGN detects heavily occluded objects more reliably by leveraging segmentation-guided centers, enabling consistent center estimation even from partial surfaces and improving box placement when large portions of objects are invisible. In crowded scenes (Fig. 4(c)), baseline detectors often struggle to separate adjacent instances due to ambiguous query initialization and overlapping receptive fields, which frequently leads to merged or misplaced detections. ALIGN mitigates this issue by initializing queries from well-separated object centers and restricting feature aggregation within object-specific regions, thereby preserving clear boundaries and improving instance separation. Finally, Fig. 4(d) demonstrates improved detection of distant and small objects, where adaptive sampling around cluster cores compensates for sparse LiDAR observations and enhances local geometric representation in low-density regions. Overall, these results show that ALIGN mitigates key failure modes—occlusion, crowding,

and distance—through a unified, geometry-aware query initialization framework.

5 Conclusion

We presented **ALIGN**, a structured query-initialization framework that integrates geometric and semantic cues for multi-modal 3D object detection. While prior sampling strategies either distribute queries uniformly or focus on clearly visible regions, often missing small or occluded objects, ALIGN aligns LiDAR geometry with image semantics to guide balanced and object-aware query placement across foreground and background regions. By integrating OCE, ANS, and DQB, ALIGN enforces spatial consistency and yields more stable query distributions with stronger cross-modal alignment. Extensive experiments demonstrate that ALIGN consistently improves performance across multiple detectors, with particularly large gains under low-visibility conditions. These results show that improving the initialization stage alone can deliver reliable performance gains without modifying detector architectures. Although ALIGN introduces additional computation and partially depends on segmentation quality in OCE, these are practical rather than fundamental limitations and can be mitigated through lightweight segmentation or self-supervised geometric estimation. Overall, this work takes a clear step toward more structured and object-aware query initialization, highlighting the importance of geometry–semantic alignment for robust perception in complex driving scenes.

Supplementary Material

ALIGN: Advanced Query Initialization with LiDAR-Image Guidance for Occlusion-Robust 3D Object Detection

A Class-Specific Depth Offset in OCE.

In the Occlusion-aware Center Estimation (OCE) module, object centers are initialized by projecting LiDAR points onto the image plane and computing a representative surface point p_{surf} from image-guided segmentation. However, since LiDAR sensors only capture visible surfaces, the recovered 3D point typically lies on the front-facing surface of an object rather than at its geometric center. This leads to a systematic depth bias, where the estimated center is consistently shifted toward the camera, especially for elongated or partially occluded objects.

To address this limitation, we introduce a depth offset d along the LiDAR ray direction, which shifts the surface point deeper into the scene to better approximate the true object center. Crucially, this offset is not treated as a free hyper-parameter. Instead, following [Ji *et al.*, 2024], we derive class-specific offset ranges from dataset-level object size statistics.

Specifically, we compute the empirical distributions of object width, height, and length for each category and estimate the expected distance between the visible surface and the geometric center. As a result, large and elongated objects require larger offsets, while compact or symmetric ones need only minimal adjustment.

Table 7 summarizes the resulting class-wise size statistics and the derived depth offset ranges. These values are fixed during inference and introduce no additional learnable parameters. As shown in Table 8, the proposed class-specific depth offsets consistently reduce Average Scale Error (ASE) and Average Orientation Error (AOE), confirming that this data-driven compensation improves the geometric quality of 3D bounding box estimation.

Category	(w_{\min}, w_{\max})	(h_{\min}, h_{\max})	(l_{\min}, l_{\max})	(d_{\min}, d_{\max})
Car	(1.4, 2.8)	(1.2, 3.1)	(3.4, 6.6)	(0.6, 3.9)
Pedestrian	(0.3, 1.0)	(1.0, 2.2)	(0.3, 1.3)	(0.2, 1.4)
Bus	(2.6, 3.5)	(2.8, 4.6)	(6.9, 13.8)	(1.3, 7.5)
Truck	(1.7, 3.5)	(1.7, 4.5)	(4.5, 14.0)	(0.8, 7.6)
Trailer	(2.2, 2.3)	(3.3, 3.9)	(1.7, 14.0)	(0.8, 7.4)
Constr. veh.	(2.1, 3.4)	(2.0, 3.0)	(3.7, 7.6)	(1.0, 4.4)
Motorcycle	(0.4, 1.5)	(1.1, 2.0)	(1.2, 2.8)	(0.2, 1.9)
Bicycle	(0.4, 0.9)	(0.9, 2.0)	(1.3, 2.0)	(0.2, 1.5)
Traffic cone	(0.2, 1.2)	(0.5, 1.4)	(1.3, 2.0)	(0.1, 1.4)
Barrier	(1.7, 3.6)	(0.8, 1.4)	(0.3, 0.8)	(0.2, 2.0)

Table 7: Per-class bounding box size ranges and corresponding depth offset ranges used in OCE. Each prior is computed from dataset-level statistics and reflects the expected distance between the visible surface and the true object center, helping compensate for depth bias. All values are in meters.

B Details of Object Center Estimation in OCE

OCE estimates each object’s 3D center by geometrically linking image-space object cues with LiDAR measurements. From each camera view, the segmentation network identifies object regions and computes their 2D centroids, which serve as approximate object centers in image space. Given a 2D centroid (u_c, v_c) , we project it into the LiDAR coordinate system using the calibrated camera–LiDAR transformation.

To obtain a 3D estimate, we associate the projected image center with a local set of LiDAR points inside the same segmented region. Specifically, we collect a small set of neighboring LiDAR points $\mathcal{S} = \{\mathbf{P}_1, \mathbf{P}_2, \mathbf{P}_3, \mathbf{P}_4\}$ and use them to define a local geometric mapping from the image plane to the LiDAR space. This transformation yields a geometry-consistent estimate of the visible surface location corresponding to the image centroid, denoted as $\mathbf{C}'_{\text{2Dbbox}}$ in Fig. 5.

Since LiDAR observes only the visible surface of an object, the resulting 3D point typically lies on the front-facing surface rather than at the true geometric center, especially for elongated or partially occluded objects. To compensate for this systematic depth bias, OCE applies a depth offset d along the viewing direction, shifting the surface point deeper into the scene. \mathbf{v} denotes the viewing direction.

$$\mathbf{C}_{\text{3Dbbox}} = \mathbf{C}'_{\text{2Dbbox}} + d \cdot \mathbf{v},$$

The offset value is determined empirically from dataset-level object size statistics and remains fixed during inference. This simple geometric correction introduces no additional learnable parameters and incurs negligible computational cost. Despite its simplicity, it aligns the image-derived center with the LiDAR’s 3D structure, improving the spatial accuracy of query initialization and enabling robust detection of small or partially occluded objects.

C Details of LiDAR Clustering in ANS

In the Adaptive Neighbor Sampling (ANS) module, object candidates are extracted by applying DBSCAN [Schubert *et al.*, 2017] to LiDAR points within a predefined region-of-interest (ROI). We use a fixed parameters $\text{eps} = 0.6$ and a minimum cluster size $\text{minPts} = 7$ for all scenes.

These parameters follow the commonly adopted clustering settings used for nuScenes LiDAR data and are kept fixed across all experiments. In practice, we found that ANS is not highly sensitive to moderate variations of these values, as its role is not to produce precise object segmentation but to provide coarse object proposals for query initialization. As long as clusters roughly capture object-scale point groups, the subsequent transformer decoding can refine localization.

To accelerate clustering, we utilize the GPU-based DBSCAN implementation from NVIDIA’s cuML library [Raschka *et al.*, 2020]. Since LiDAR points are already represented as PyTorch [Paszke *et al.*, 2019] tensors

Method	Metric	Car	Truck	Bus	Tra.	Const.	Ped.	Moto.	Bike	Cone	Bar.	Total
CMT	ASE(\downarrow)	14.0	17.8	16.8	21.8	44.8	27.6	23.1	25.7	31.5	27.1	25.0
		14.0	17.9	16.7	21.7	44.5	27.5	22.3	25.1	30.9	27.1	24.7 (-0.3)
CMT	AOE(\downarrow)	4.00	4.20	4.00	35.9	83.6	28.5	22.0	30.2	—	4.30	24.1
		3.80	3.80	4.00	33.8	79.8	26.9	20.1	27.2	—	4.10	22.6 (-1.5)

Table 8: Class-specific depth offsets improve ASE and AOE on the nuScenes validation set.

Model	Lat. (ms)	Mem. (MB)	mAP	NDS
<i>No segmentation (baseline)</i>	163	2812	67.4	70.2
RDRNet-s	237 (+38)	4275	67.8 (+0.4)	70.3 (+0.1)
YOLACT	346 (+147)	4707	67.7 (+0.3)	70.2 (-)
Cascade Mask R-CNN	588 (+389)	5414	67.9 (+0.5)	70.5 (+0.3)
SOLOv2	465 (+266)	6984	67.9 (+0.5)	70.5 (+0.3)
Mask R-CNN	190 (+27)	4066	68.0 (+0.6)	70.8 (+0.6)

Table 9: Effect of segmentation model choice in OCE on computational cost and detection performance. Results are measured on the nuScenes validation set using CMT-small as the base detector.

on the GPU, we convert them to the cuML format using DLpack [DLPack Contributors, 2020]-based zero-copy transformation. On a single NVIDIA A6000 Ada GPU, DBSCAN clustering for one nuScenes scene takes only 27ms, achieving over 50 \times speedup compared to the CPU version. Although the clustering step introduces additional computation, its overhead remains small and does not affect real-time inference.

D Segmentation Model Comparison

To analyze the dependence of OCE on the segmentation backbone, we evaluate several pretrained instance segmentation models from MMDetection, including Mask R-CNN [He *et al.*, 2017], Cascade Mask R-CNN [Cai and Vasconcelos, 2019], YOLACT [Bolya *et al.*, 2019], SOLOv2 [Wang *et al.*, 2020], and the real-time model RDRNet [Yang *et al.*, 2024]. All models are fine-tuned on the nuImages dataset using their released pretrained weights and original training configurations.

For a fair comparison, each model processes six multi-view images from nuScenes, and both GPU memory consumption and inference latency are measured on a single NVIDIA A6000 Ada GPU. Mask R-CNN shares the image backbone with the base detector as described in the main paper, while the other segmentation models are evaluated as standalone networks and fine-tuned for three epochs on nuImages for performance comparison. As a result, their latency and memory overhead are higher, which reflects the cost of using independent segmentation backbones rather than a shared feature extractor.

Table 9 reports the results on the nuScenes validation set using CMT-Large as the base detector. The first row shows the baseline that applies only ANS without segmentation guidance. Although heavier segmentation networks incur significantly higher computational cost, their detection accuracy gains remain marginal. In contrast, the lightweight RDRNet-S achieves comparable mAP and NDS with substantially lower latency and memory usage.

Importantly, across all settings, incorporating OCE consistently improves performance over the baseline, even when lightweight or real-time segmentation models are used. This indicates that OCE does not critically depend on highly accurate or finely detailed segmentation masks. While precise instance segmentation is beneficial, our results show that coarse object-level masks are already sufficient to provide reliable geometric cues for center initialization. In practice, what matters most is whether the segmentation successfully identifies the presence of an object region, rather than how precisely its boundary is delineated.

These results suggest that OCE is robust to moderate segmentation noise and remains effective as long as rough object regions can be recovered. The main performance gains stem from geometric alignment and localized query initialization, which remain stable even under imperfect segmentation, alleviating concerns about brittleness in adverse conditions such as rain, motion blur, or distant objects.

E More Visualization Results

Figure 6 shows qualitative comparisons between the ground truth, the CMT baseline, and CMT with ALIGN on challenging scenes with heavy occlusion and crowding.

In (a), a BEV-level comparison illustrates that while nearby vehicles and bicycles are detected similarly across models, the baseline often misses or mislocalizes partially occluded or distant objects such as barriers and pedestrians. In contrast, ALIGN more reliably recovers these occluded instances and produces more accurate bounding boxes in the highlighted regions. In (b), image-view results further show that CMT fails to localize pedestrians partially hidden behind vehicles or street furniture, whereas ALIGN successfully detects these occluded pedestrians. In (c), crowded scenes with overlapping objects remain challenging for the baseline, which often produces incomplete or fragmented detections. ALIGN, however, yields more stable and coherent predictions in such dense environments.

Overall, these results demonstrate that ALIGN substantially improves detection robustness under occlusion and crowding through geometry-aware query initialization. Nevertheless, extremely small and thin objects such as distant traffic cones remain challenging due to limited visual and geometric cues, leaving room for future improvement.

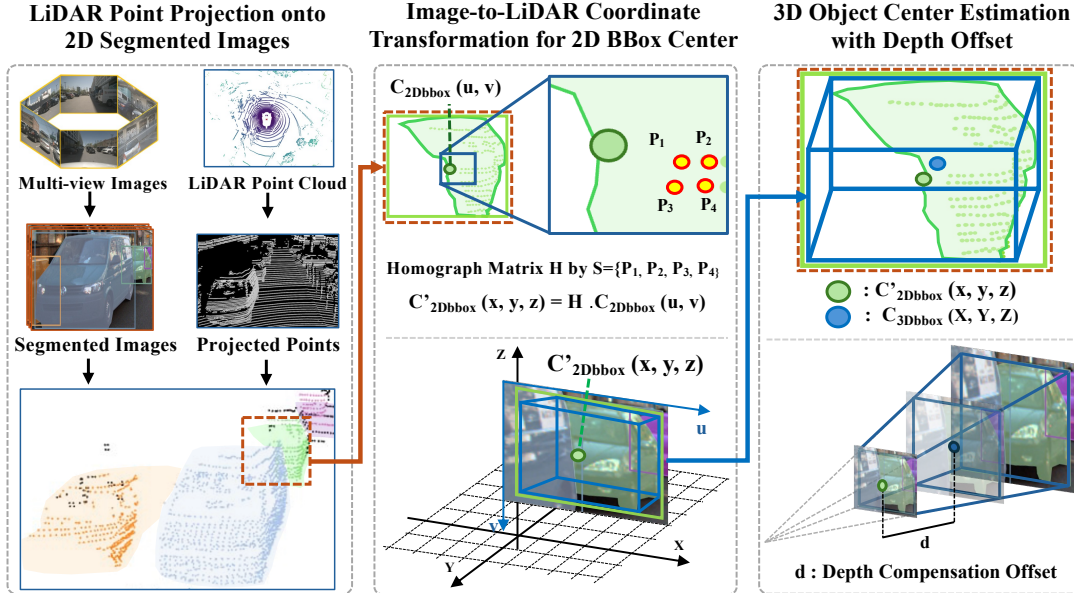


Figure 5: **Visualization of 3D object center estimation in OCE.** The 2D center from segmentation is projected to the LiDAR frame and refined with a depth offset for geometry-consistent query initialization.

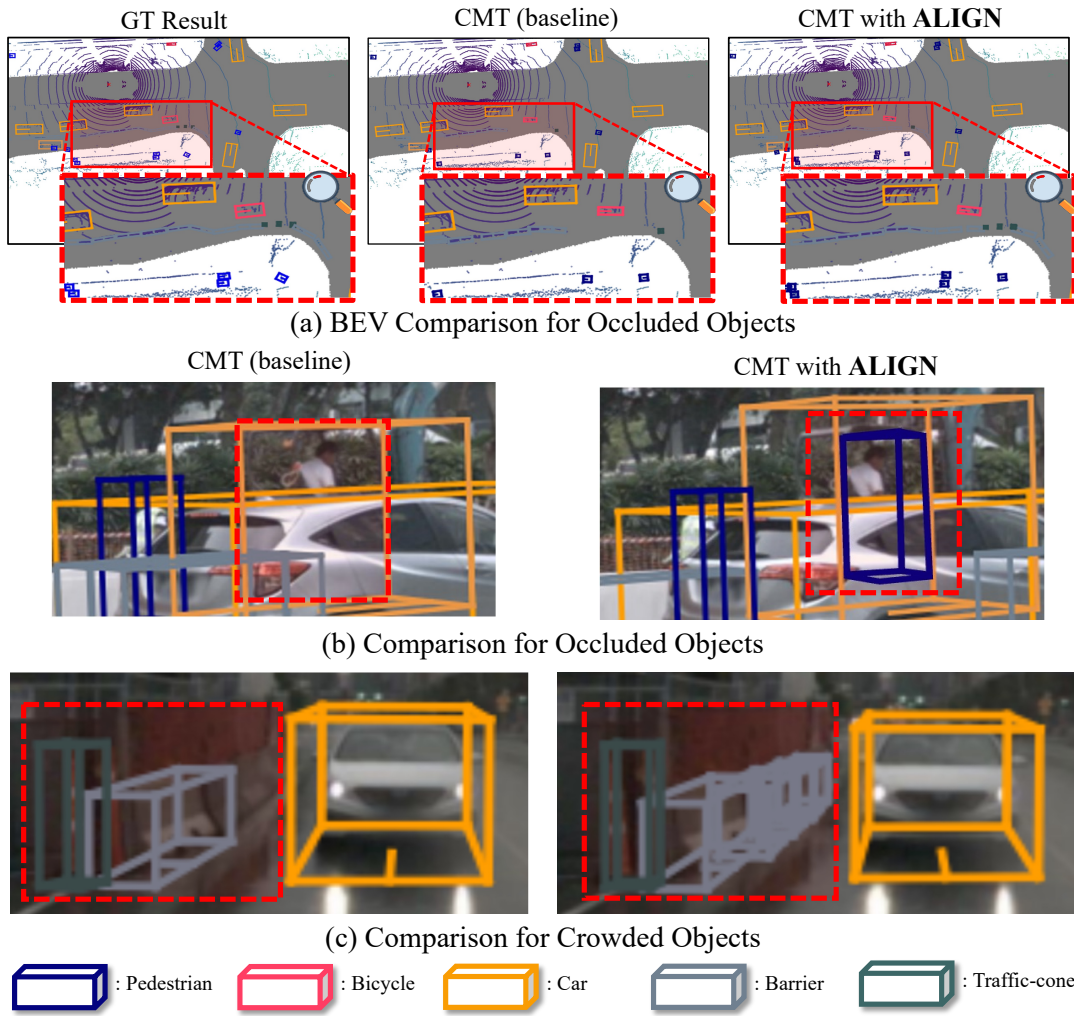


Figure 6: **Qualitative results on occluded and crowded scenes**

References

- [Bai *et al.*, 2022] Xuyang Bai, Zeyu Hu, Xinge Zhu, Qingqiu Huang, Yilun Chen, Hangbo Fu, and Chiew-Lan Tai. TransFusion: Robust LiDAR-Camera Fusion for 3D Object Detection with Transformers. In *2022 IEEE/CVF Conference on Computer Vision and Pattern Recognition (CVPR)*, pages 1080–1089, New Orleans, LA, USA, June 2022. IEEE.
- [Bolya *et al.*, 2019] Daniel Bolya, Chong Zhou, Fanyi Xiao, and Yong Jae Lee. Yolact: Real-time instance segmentation. In *Proceedings of the IEEE/CVF international conference on computer vision*, pages 9157–9166, 2019.
- [Caesar *et al.*, 2020] Holger Caesar, Varun Bankiti, Alex H. Lang, Sourabh Vora, Venice Erin Liang, Qiang Xu, Anush Krishnan, Yu Pan, Giancarlo Baldan, and Oscar Beijbom. nuScenes: A Multimodal Dataset for Autonomous Driving. In *2020 IEEE/CVF Conference on Computer Vision and Pattern Recognition (CVPR)*, pages 11618–11628, Seattle, WA, USA, June 2020. IEEE.
- [Cai and Vasconcelos, 2019] Zhaowei Cai and Nuno Vasconcelos. Cascade r-cnn: High quality object detection and instance segmentation. *IEEE transactions on pattern analysis and machine intelligence*, 43(5):1483–1498, 2019.
- [Carion *et al.*, 2020] Nicolas Carion, Francisco Massa, Gabriel Synnaeve, Nicolas Usunier, Alexander Kirillov, and Sergey Zagoruyko. End-to-end object detection with transformers. In *European conference on computer vision*, pages 213–229. Springer, 2020.
- [Chen *et al.*, 2022a] Xuanyao Chen, Tianyuan Zhang, Yue Wang, Yilun Wang, and Hang Zhao. FUTR3D: A Unified Sensor Fusion Framework for 3D Detection, March 2022. Issue: arXiv:2203.10642 arXiv:2203.10642 [cs].
- [Chen *et al.*, 2022b] Zehui Chen, Zhenyu Li, Shiquan Zhang, Liangji Fang, Qinhong Jiang, and Feng Zhao. Deformable feature aggregation for dynamic multi-modal 3d object detection. In *European conference on computer vision*, pages 628–644. Springer, 2022.
- [Chen *et al.*, 2023a] Xuanyao Chen, Tianyuan Zhang, Yue Wang, Yilun Wang, and Hang Zhao. FUTR3D: A Unified Sensor Fusion Framework for 3D Detection. In *Proceedings of the IEEE/CVF Conference on Computer Vision and Pattern Recognition (CVPR) Workshops*, pages 172–181, 2023.
- [Chen *et al.*, 2023b] Yilun Chen, Zhiding Yu, Yukang Chen, Shiyi Lan, Anima Anandkumar, Jiaya Jia, and Jose M Alvarez. Focalformer3d: focusing on hard instance for 3d object detection. In *Proceedings of the IEEE/CVF International Conference on Computer Vision*, pages 8394–8405, 2023.
- [DLPack Contributors, 2020] DLPack Contributors. DLPack: Open In-Memory Tensor Structure. <https://github.com/dmlc/dlpack>, 2020.
- [Gao *et al.*, 2022] Ziteng Gao, Limin Wang, Bing Han, and Sheng Guo. Adamixer: A fast-converging query-based object detector. In *Proceedings of the IEEE/CVF Conference on Computer Vision and Pattern Recognition*, pages 5364–5373, 2022.
- [Gong *et al.*, 2025] Bowen Gong, Yimeng Wang, Ciyun Lin, and Hongchao Liu. Roadside lidar-camera fusion detection based on spatiotemporal calibration. *IEEE Sensors Journal*, 2025.
- [He and Todorovic, 2022] Liqiang He and Sinisa Todorovic. Destr: Object detection with split transformer. In *Proceedings of the IEEE/CVF conference on computer vision and pattern recognition*, pages 9377–9386, 2022.
- [He *et al.*, 2017] Kaiming He, Georgia Gkioxari, Piotr Dollár, and Ross Girshick. Mask r-cnn. In *Proceedings of the IEEE international conference on computer vision*, pages 2961–2969, 2017.
- [Huang *et al.*, 2024] Junjie Huang, Yun Ye, Zhujin Liang, Yi Shan, and Dalong Du. Detecting as labeling: Rethinking lidar-camera fusion in 3d object detection. In *European Conference on Computer Vision*, pages 439–455. Springer, 2024.
- [Ji *et al.*, 2024] Haoxuanye Ji, Pengpeng Liang, and Erkang Cheng. Enhancing 3d object detection with 2d detection-guided query anchors. In *Proceedings of the IEEE/CVF Conference on Computer Vision and Pattern Recognition*, pages 21178–21187, 2024.
- [Kuhn, 1955] H. W. Kuhn. The Hungarian method for the assignment problem. *Naval Research Logistics Quarterly*, 2(1-2):83–97, 1955.
- [Li *et al.*, 2022] Yanwei Li, Yilun Chen, Xiaojuan Qi, Zeming Li, Jian Sun, and Jiaya Jia. Unifying Voxel-based Representation with Transformer for 3D Object Detection, October 2022. Issue: arXiv:2206.00630 arXiv:2206.00630 [cs].
- [Liang *et al.*, 2018] Ming Liang, Bin Yang, Shenlong Wang, and Raquel Urtasun. Deep Continuous Fusion for Multi-sensor 3D Object Detection. In *Computer Vision – ECCV 2018*, volume 11220, pages 663–678. Springer International Publishing, Cham, 2018.
- [Lin *et al.*, 2017] Tsung-Yi Lin, Priya Goyal, Ross Girshick, Kaiming He, and Piotr Dollar. Focal Loss for Dense Object Detection. In *Proceedings of the IEEE International Conference on Computer Vision*, pages 2980–2988, 2017.
- [Liu *et al.*, 2022a] Yingfei Liu, Tiancai Wang, Xiangyu Zhang, and Jian Sun. PETR: Position Embedding Transformation for Multi-View 3D Object Detection, July 2022. Issue: arXiv:2203.05625 arXiv:2203.05625 [cs].
- [Liu *et al.*, 2022b] Zhijian Liu, Haotian Tang, Alexander Amini, Xinyu Yang, Huizi Mao, Daniela Rus, and Song Han. BEVFusion: Multi-Task Multi-Sensor Fusion with Unified Bird’s-Eye View Representation, June 2022. Issue: arXiv:2205.13542 arXiv:2205.13542 [cs].
- [Loshchilov and Hutter, 2019] Ilya Loshchilov and Frank Hutter. Decoupled weight decay regularization, 2019.
- [Paszke *et al.*, 2019] Adam Paszke, Sam Gross, Francisco Massa, Adam Lerer, James Bradbury, Gregory Chanan,

- Trevor Killeen, Zeming Lin, Natalia Gimelshein, Luca Antiga, et al. Pytorch: An imperative style, high-performance deep learning library. *Advances in neural information processing systems*, 32, 2019.
- [Raschka *et al.*, 2020] Sebastian Raschka, Joshua Patterson, and Corey Nolet. Machine learning in python: Main developments and technology trends in data science, machine learning, and artificial intelligence. *arXiv preprint arXiv:2002.04803*, 2020.
- [Schubert *et al.*, 2017] Erich Schubert, Jörg Sander, Martin Ester, Hans Peter Kriegel, and Xiaowei Xu. Dbscan revisited, revisited: why and how you should (still) use db-scan. *ACM Transactions on Database Systems (TODS)*, 42(3):1–21, 2017.
- [Smith, 2017] Leslie N. Smith. Cyclical Learning Rates for Training Neural Networks, April 2017. Issue: arXiv:1506.01186 arXiv:1506.01186 [cs].
- [Van Geerenstein *et al.*, 2024] Mathijs R Van Geerenstein, Felicia Ruppel, Klaus Dietmayer, and Dariu M Gavrila. Multimodal object query initialization for 3d object detection. In *2024 IEEE International Conference on Robotics and Automation (ICRA)*, pages 12484–12491. IEEE, 2024.
- [Wang *et al.*, 2020] Xinlong Wang, Rufeng Zhang, Tao Kong, Lei Li, and Chunhua Shen. Solov2: Dynamic and fast instance segmentation. *Advances in Neural information processing systems*, 33:17721–17732, 2020.
- [Wang *et al.*, 2022] Yue Wang, Vitor Campagnolo Guizilini, Tianyuan Zhang, Yilun Wang, Hang Zhao, and Justin Solomon. Detr3d: 3d object detection from multi-view images via 3d-to-2d queries. In *Conference on Robot Learning*, pages 180–191. PMLR, 2022.
- [Wang *et al.*, 2023] Zitian Wang, Zehao Huang, Jiahui Fu, Naiyan Wang, and Si Liu. Object as query: Lifting any 2d object detector to 3d detection, 2023.
- [Xie *et al.*, 2023] Yichen Xie, Chenfeng Xu, Marie-Julie Rakotosaona, Patrick Rim, Federico Tombari, Kurt Keutzer, Masayoshi Tomizuka, and Wei Zhan. Sparse-fusion: Fusing multi-modal sparse representations for multi-sensor 3d object detection. In *Proceedings of the IEEE/CVF International Conference on Computer Vision*, pages 17591–17602, 2023.
- [Yan *et al.*, 2023a] Junjie Yan, Yingfei Liu, Jianjian Sun, Fan Jia, Shuailin Li, Tiancai Wang, and Xiangyu Zhang. Cross modal transformer: Towards fast and robust 3d object detection, 2023.
- [Yan *et al.*, 2023b] Junjie Yan, Yingfei Liu, Jianjian Sun, Fan Jia, Shuailin Li, Tiancai Wang, and Xiangyu Zhang. Cross Modal Transformer via Coordinates Encoding for 3D Object Detection, January 2023. Issue: arXiv:2301.01283 arXiv:2301.01283 [cs].
- [Yang *et al.*, 2024] Guoyu Yang, Yuan Wang, and Daming Shi. Reparameterizable dual-resolution network for real-time semantic segmentation. *arXiv preprint arXiv:2406.12496*, 2024.
- [Zhang *et al.*, 2024] Hongcheng Zhang, Liu Liang, Pengxin Zeng, Xiao Song, and Zhe Wang. Sparselif: High-performance sparse lidar-camera fusion for 3d object detection. In *European Conference on Computer Vision*, pages 109–128. Springer, 2024.
- [Zhao *et al.*, 2024] Yian Zhao, Wenyu Lv, Shangliang Xu, Jinman Wei, Guanzhong Wang, Qingqing Dang, Yi Liu, and Jie Chen. Detrs beat yolos on real-time object detection. In *Proceedings of the IEEE/CVF Conference on Computer Vision and Pattern Recognition*, pages 16965–16974, 2024.
- [Zhou *et al.*, 2022] Zixiang Zhou, Xiangchen Zhao, Yu Wang, Panqu Wang, and Hassan Foroosh. CenterFormer: Center-Based Transformer for 3D Object Detection. *Computer Vision – ECCV 2022*, 13698:496–513, 2022.
- [Zhu *et al.*, 2019] Benjin Zhu, Zhengkai Jiang, Xiangxin Zhou, Zeming Li, and Gang Yu. Class-balanced Grouping and Sampling for Point Cloud 3D Object Detection, August 2019. Issue: arXiv:1908.09492 arXiv:1908.09492 [cs].
- [Zhu *et al.*, 2021] Xizhou Zhu, Weijie Su, Lewei Lu, Bin Li, Xiaogang Wang, and Jifeng Dai. Deformable DETR: Deformable Transformers for End-to-End Object Detection. In *International Conference on Learning Representations (ICLR)*, 2021.